Reaction Chemistry & Engineering

Bayesian Optimization of Electrochemical Devices for Electrons-to-Molecules Conversions: The Case of Pulsed CO2 Electroreduction

Journal:	*Reaction Chemistry & Engineering*
Manuscript ID	RE-ART-07-2022-000285.R2
Article Type:	Paper
Date Submitted by the Author:	04-Oct-2022
Complete List of Authors:	Frey, Daniel; New York University Tandon School of Engineering, Chemical and Biological Engineering Neyerlin, K.; National Renewable Energy Laboratory, Chemical and Materials Science and Technology Modestino, Miguel; New York University Tandon School of Engineering, Chemical and Biological Engineering

ARTICLE

Bayesian Optimization of Electrochemical Devices for Electrons-to-Molecules Conversions: The Case of Pulsed CO_2 Electroreduction†

Received 00th January 20xx,
Accepted 00th January 20xx

DOI: 10.1039/x0xx00000x

Daniel Frey[a], K.C. Neyerlin[b,*], and Miguel A. Modestino*[a]

Electrons-to-molecules conversions have emerged as a route to integrate renewable electricity into chemical production processes and ultimately contribute to the decarbonization of chemistry. The practical implementation of these conversions will depend on the optimization of many electrolyzer design and operating parameters. Bayesian optimization (BO) has been shown to be a robust and efficient method for these types of optimization problems where data may be scarce. Here, we demonstrate the use of BO to improve a membrane electrode assembly (MEA) CO_2 electrolyzer, targeting the production of CO through dynamic operation. In a system with intentionally unoptimized components, we first demonstrate the effectiveness of dynamic voltage pulses on CO Faradaic efficiency (FE), then utilize BO for 3D and 4D optimization of pulse times and current densities to increase CO partial current density by >64% from the initially tested conditions. The methodology showcased here lays the groundwork for the optimization of other complex electrons-to-molecules conversions that will be required for the electrification of chemical manufacturing.

Introduction

High-performing electrochemical reactors could enable electrification and subsequent decarbonization of the chemical industry,[1-4] a sector responsible for 7% of the global greenhouse gas (GHG) emissions and 10% of the worlds energy, primarily in the form heat derived from fossil-fuel-combustion.[5, 6] Deploying electrochemical processes to replace current thermochemical routes of chemical production relies on the development of continuous reactors that operate at high-throughput, selectivity, energy conversion efficiency, and leverage low-cost chemical feedstocks. To accelerate the development of such reactors, rapid optimization approaches are needed to identify conditions of operation that maximize their performance. Optimizing these types of reactors is challenging because of the large number of design (*e.g.*, electrocatalyst compositions, device geometries, membrane chemistry) and operating parameters (*e.g.*, temperatures, potentials, flowrates, pressure and their dynamic modulation), which often results in an intractable experimental design space. A promising data-driven optimization strategy to identify global optima with the minimum amount of experimental input is Bayesian Optimization (BO).[7-14] BO methods for reactor optimization rely on a surrogate model to statistically predict the mean and uncertainty of a desired performance metric for any possible combination of operating parameters. These surrogate models are then used to decide what experiments will provide the most information from the reactors and allow the identification of the optimum conditions with the minimum number of experiments.[15] Many areas of the chemical sciences have started to use BO to accelerate optimization campaigns, including applications in materials discovery,[16-26] design of chemical reactions,[27-37] and device optimization.[38-41] In this study, we demonstrate a general methodology to optimize the operation of electrochemical conversion devices for chemical manufacturing, using dynamic CO_2 electroreduction to CO as a model reaction. This model reaction was chosen (i) because its optimization may lead to a path to upconvert CO_2 into useful products and possibly reduce carbon emissions,[42-47] (ii) because stable and efficient silver (Ag) electrocatalysts have been widely studied,[48-61] and (iii) because learnings from this reaction can be translated to the optimization methodology of other emerging electrochemical conversion processes of relevance to chemical manufacturing (e.g., ethylene or propylene production and functionalization).[62-68]

To demonstrate the effectiveness of BO in optimizing CO_2 electroreduction, we developed a methodology to maximize CO production under dynamic potential pulsing with current densities and pulse times as optimization parameters. Pulsed potentials, and resultingly current density, can elicit favorable transient behavior, affecting hydrodynamics, the electrocatalyst double layer, reactant concentration, and the presence or absence of different intermediates and adsorbates on the electrode surface microenvironment.[69-71] More specifically, previous studies have shown that the use of dynamic voltage pulses can control selectivity and/or stability of

[a.] New York University, Tandon School of Engineering, Department of Chemical and Biomolecular Engineering, 6 Metrotech Center, Brooklyn, NY, E-mail: modestino@nyu.edu; Tel: +1 646-997-3594
[b.] National Renewable Energy Laboratory, Chemistry and Nanoscience Center, Golden, CO, E-mail: kenneth.neyerlin@nrel.gov

† Electronic Supplementary Information (ESI) available: Acquisition function descriptions, objective function descriptions, and supplementary results. See DOI: 10.1039/x0xx00000x

CO_2 electroreduction.[56, 72-84] All of these studies used a systematic approach to determine optimal operation conditions leading to large information gaps between the tested experimental conditions and possibly sub-optimal parameter selection. In this study, we leverage these previous findings to demonstrate the use of BO to rapidly optimize the dynamic operating conditions in industrially relevant zero-gap electrochemical conversion devices. Our findings demonstrate the ability to map performance metrics in large design spaces with high accuracy while also identifying optimal operation strategies with a low number of experiments.

Experimental

Preparation of Catalyst Inks

BO The cathode catalyst inks were prepared by mixing commercial Vulcan supported Ag (40%, Fuel Cell Store), deionized water, n-propyl alcohol (nPA), and ionomer (5 wt% Sustainion XA-9, Dioxide Materials). The ratio of ionomer, catalyst, and Vulcan for the cathode ink was 1:2.6:4. The anode catalyst inks were prepared by mixing commercial Iridium(IV) oxide (Premion 99.99%, Alfa Aesar), deionized water, nPA, and 10 wt% PFAEM ionomer(84) together. The ratio of ionomer and catalyst for the anode ink was 1:6.6. For both anode and cathode inks, the ink was dispersed first with a horn sonicator for 20 seconds, and then sonicated in an ice bath for 30 minutes.

Catalyst GDE Fabrication

For the cathode GDE, a GDL (Sigracet 29BC, Fuel Cell Store) with a thickness of 235 µm ± 25 µm was placed on a heated vacuum table at 80°C with the micro porous layer (MPL) facing up. The catalyst ink was ultrasonically sprayed onto the GDL using an automatic Sonotek Spray System. The spray pattern was serpentine, switching orientations after each pass. For the anode GDE, the same procedure was used except the GDL was Toray Paper 060 (5% wet proofing, Fuel Cell Store). The nominal cathode loading was 5 mg/cm^2 and the nominal anode loading was 4 mg/cm^2.

Electrochemical Reactor Configuration and Operation

A custom-built hardware with 25 cm^2 active area was used to evaluate the performance of the electrochemical reduction of CO_2. The anode GDE with area of 25 cm^2 with a thickness of 0.009 inches was placed against the anode flow field with triple serpentine flow channels and was compressed to 18% using 0.008 inches of polytetrafluoroethylene (PTFE) gaskets. A commercial anion exchange membrane (AEM) (Aemion, 25µm, Ionomr Innovations Inc.) was placed next to the anode GDE. A cathode GDE with 25 cm^2 active area was placed against the membrane, sealed with PTFE gaskets, and was compressed to 18% once the cell was tightened to 40 inch-pound. The endplates of the cell were heated to 60°C and the temperature was kept constant for all experiments. The flow plates for cathode and anode were made from Ti and had 25 cm^2 area of triple serpentine flow channels. The CO_2 gas stream was heated to 60°C and was delivered to the cathode GDE through the cathode flow plate at a constant flow rate of 1 L min^{-1}. 1 M potassium hydroxide (KOH) electrolyte made by dissolving KOH pellets (Certified ACS, VWR) in 18 MΩ cm deionized water was heated to 60°C and fed to the anode flow plate at 50 mL min^{-1}. A Gamry Reference 3000 Potentiostat with a Reference 30K Booster was used for the electrochemical measurements. Galvanodynamic polarizations were conducted from 0 to 400 mA cm^{-2} at a rate of 5 mA cm^{-2} s^{-1}. For constant current and pulse experiments, the different current density settings were held for at least 120 s before gas product samples were taken and analyzed. To avoid systematic errors from long-term degradation of the catalyst layer, the cathode catalyst layer was replaced every 20 experiments. Each set of 20 experiments consisted of 10 different reactor operation conditions repeated twice. In addition, two identical experimental conditions were repeated with each of the catalyst layers to monitor possible deviation between different experimental sets.

Product Analysis

The effluent of the gas stream from the cathode flow plate was separated from the liquid effluent using a gas trap. Gas samples were analyzed in a 4900 Micro GC (10m, molecular sieve, Agilent). Samples were collected in Supel™ Inert Multi-Layer Foil Gas Sampling Bags (Sigma-Aldrich) for a recorded time (30 s) and manually inserted into the Micro GC with an injection time of 100 µs. The injection temperature was set to 110°C. Carbon monoxide (CO) was detected using a 10 m MS5A column, heated (105°C) and pressurized (28 psi) with Argon as carrier gas (Matheson Gas- Matheson Purity). The compounds were detected on an integrated thermal conductivity detector (TCD).

Bayesian Optimization Process

The Bayesian optimization (BO) process used in this study was based on the BO algorithm used in Frey et al.[2] BO algorithms consist of two main components: a surrogate model (SM) and an acquisition function. The SM is used to predict the value of the experimental objective function for any set of experimental conditions, $\boldsymbol{x}$. $\boldsymbol{x}$ is bounded by lower and upper bounds for each dimension, $\boldsymbol{x}_{LB}$ and $\boldsymbol{x}_{UB}$, which are arrays of the same dimensionality of $\boldsymbol{x}$. For example, for the two-dimensional (2D) design space used in this study (active pulse time and resting pulse time), the $\boldsymbol{x}_{LB}$ was [10 ms, 10 ms] and the $\boldsymbol{x}_{UB}$ was [1500 ms, 1500 ms]. The SM was trained using the experimental evaluations of the experimental objective function. As the SM in this study we use a Gaussian process regressor (GPR) using the radial basis function (RBF) kernel with noise added to the experimental values. The RBF kernel equation is:

$$k(x_i,x_j) = exp\left(-\frac{d(x_i,x_j)^2}{2l^2}\right)$$

where x_i and x_j are any two locations in the design space, d is the Euclidean distance between the two locations, and l is a length scale parameter that is optimized by the GPR algorithm. The added noise was calculated as:

$$k(x_i,x_j) = noise\_level \text{ if} x_i == x_j \text{ else } 0$$

meaning that a certain level of noise in the experimentation was assumed.

An acquisition function is used to select the next design condition(s) to evaluate based on how informative the design conditions will be in the goal of optimizing the cost function. Here, we chose to select a batch of four design conditions, as it was more convenient to run multiple experiments at one time before selecting the next batch. We used an in-house acquisition function called modified ranked-batch (MRB) which was inspired by the work of Cardoso et al..[3] In general, an acquisition function uses the current information (experimental conditions already studied) and the SM predictions to calculate how informative a possible design condition is expected to be based on the criteria for the respective acquisition function. To determine the most informative design point to sample next, a maximization method was used to find a local maximum of the acquisition function score. This process was repeated 25 times at different initiation points to ensure we achieve a value closer to the global maximum. The design point with the maximum score was subsequently added as one of the next design points to test. Multiple design points were added by repeating this acquisition function maximization step. After the new batch was selected, the experiments were performed, and the results were added to the known experimental conditions.

The MRB acquisition function calculated a score consisting of three normalized parameters: a distance score, Δ, an uncertainty score, Γ, and the objective function prediction, Ω. The distance score was calculated as:

$$\Delta = 1 - 1/\left(1 + min\sqrt{\sum_{i=1}^{d}(\boldsymbol{x_i} - \boldsymbol{x_i^{exp}})^2}\right)$$

where $min\sqrt{\sum_{i=1}^{d}(\boldsymbol{x_i} - \boldsymbol{x_i^{exp}})^2}$ is the minimum distance between the proposed set of conditions, $\boldsymbol{x}$, and each of the known sets of conditions, $\boldsymbol{x^{exp}}$. The uncertainty score, Γ, is the standard deviation of the GPR prediction at $\boldsymbol{x}$ normalized compared to the maximum and minimum observed standard deviation. The objective function prediction, Ω, is the predicted experimental objective function from the GPR at $\boldsymbol{x}$ normalized compared to the maximum and minimum observed prediction. The score that is calculated at each step in the minimization process for the respective $\boldsymbol{x}$ is:

$$\text{Score} = \beta\Delta + \beta\Gamma + \Omega$$

where β is a tradeoff value. A high value of β encourages more exploration — i.e., encourages searching unknown areas of the design space. A lower value of β encourages exploitation — i.e., searching locally near the current maximum prediction. For MRB, β changes linearly from 1 to 0 as more batches are completed.

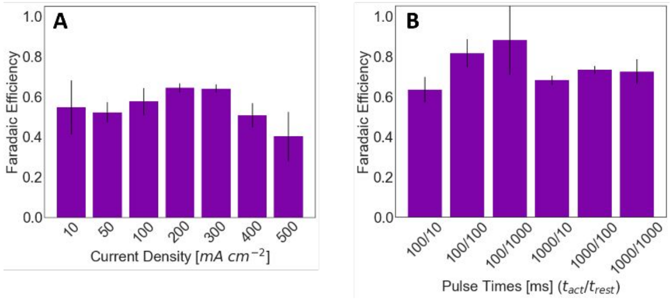

Figure 1. Faradaic efficiency of CO for (A) constant current experiments and (B) pulsed experiments. For the pulsed experiments, the active voltage was set to 3 V and the resting voltage was set to 1.1 V. The error bars indicate the standard deviation from the average of 3 experiments.

Data Availability

The code used to run this algorithm and resulting data are provided on the Github repository in reference (86).

Results

Baseline performance of CO_2 electroreduction device

To understand the baseline performance of the reactor, constant current experiments were performed to characterize the CO Faradaic efficiency (FE_{CO}). Figure 1A shows that the FE_{CO} increases with current density until 200 mA cm^{-2}, and then decreases as the current density increases to 500 mA cm^{-2}. This trend is consistent with observations from other studies on CO production on silver electrodes.[48, 51, 52, 57, 59] As an initial comparison of constant current operation versus pulsed operation, six combinations of active pulse time (t_{act}) and resting pulse time (t_{rest}) were tested. For these experiments, the active voltage was set to 3 V and the resting voltage set to 1.1 V, leading to an active total current density of 200-240 mA cm^{-2}. Our results show that FE_{CO} can be improved when appropriate pulsed potentials are applied [Figure 1(B)], as previously demonstrated in other reactor configurations[56, 69, 76, 81-83]. These initial results serve as a baseline for determining the optimal combination of active and resting pulse durations using BO.

Pulse duration effects

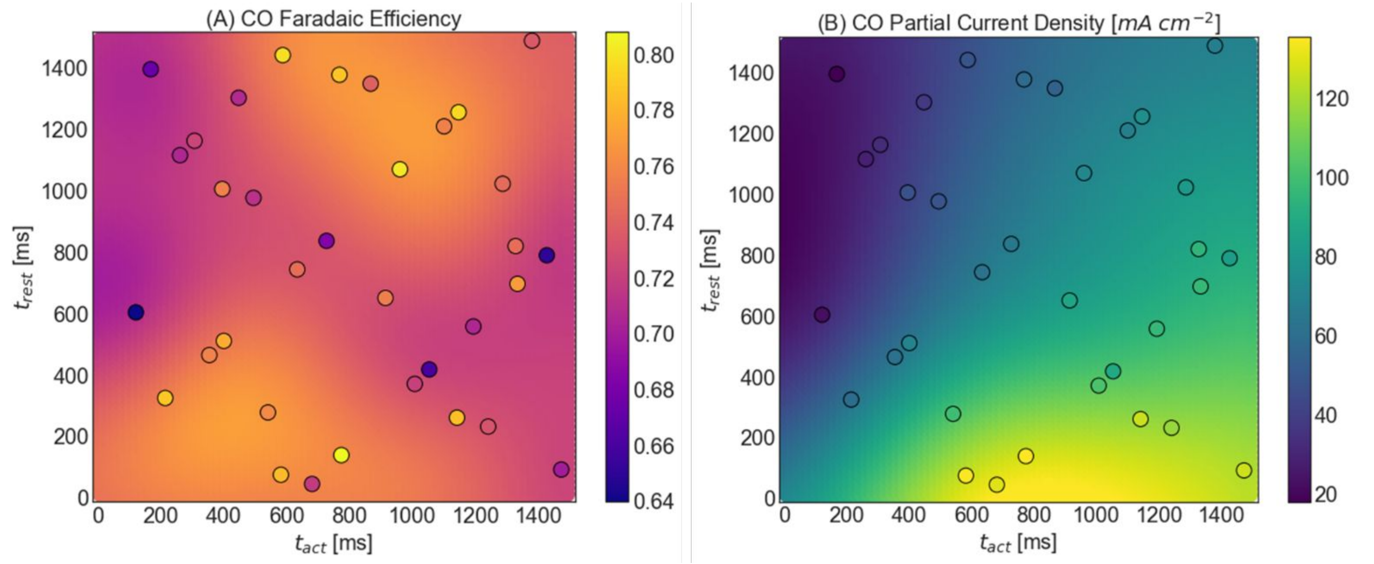

Figure 2. 2D maps of (A) FE_{CO} and (B) CO partial current density while varying t_{act} and t_{rest}. Experimental conditions are shown with a black outline. The background displays the GPR prediction based on the observed experimental values. Active current density was set to 200 mA cm^{-2} and resting current density was set to 0 mA cm^{-2}.

In order to gain insights on the effects that active pulse duration and rest pulse duration have on FE_{CO} and production rate, two-dimensional (2D) maps were constructed based on a Gaussian process regressor surrogate model (GPR SM) trained with experimental data. Figure 2 shows scatter plots of FE_{CO} and CO partial current density obtained from 34 experiments where operating conditions were randomly selected throughout the design space (*i.e.,* Pulse times in the range 10-1500 ms). The background of each plot shows the SM predictions based on the experimental data collected. Figure 2A shows the relationship between the pulse times and FE_{CO}. These results suggest that pulse time combinations with similar t_{act} and t_{rest} have the highest FE_{CO}.

Figure 2B shows that the average CO partial current density (j_{CO}) generally improves as the total active time increases. j_{CO} averages the partial current density over both the active and resting pulse times. This result is likely because longer active times allow for a larger quantity of CO_2 to be reduced, despite the fact that maximum FE_{CO} may be achieved with lower active times. To better understand the effect of the total active time on reactor performance, Figure S1 in the Support information shows FE_{CO} and j_{CO} as a function of the ratio between t_{act} and t_{rest}. As the ratio increases, the j_{CO} increases monotonically, until it reaches a value of 2.5 when it asymptotically starts to approach the limit of j_{CO} at a constant current of 200 mA cm^{-2}. This result suggests the main driver of performance is the amount time the cell is active. However, analyzing CO partial current density during the active time (j_{CO}^{act}) at various pulse time combinations (Figure S2), it is evident that longer rest duration allowed for higher j_{CO}^{act}, possibly due to an increased CO_2 concentration near the electrode. Our results identified conditions with maximum FE_{CO} of 0.79 at t_{rest} = 170 ms and t_{act} = 350 ms, and maximum j_{CO} of 126 mA cm^{-2} at t_{rest}= 10 ms and t_{act}= 830 ms. While FE_{CO} is an important metric for some applications where maintaining maximum energy efficiency is desirable, we decided to focus this study on the optimization of j_{CO} to achieve reactor operations with high throughput.

3D optimization of CO partial current density

While results presented above demonstrated the potential to modulate reactor performance by controlling pulse times, to achieve higher production rates it was important to include the current density of active pulses (j_{act}) as an optimization parameter. Given the increase in design space and the resulting requirement for larger data sets, we implemented a BO approach to identify the optimal conditions for maximum j_{CO}. A total of 50 experiments were performed in the optimization campaign in batches of four. Figure 3A shows how the experiments selected by the BO algorithm explored the entire design space initially and focused on parameters with high CO production during later stages of the search. Figure 3B shows j_{CO} during the optimization process. The maximum production rate was found at t_{rest} = 10 ms, t_{act} = 435 ms, and j_{act} = 300 mA cm^{-2} at experiment 42, leading to a j_{CO} = 189 mA cm^{-2}, representing only a small increase from the case where a constant total current density of 300 mA cm^{-2} was applied and j_{CO} = 180 mA cm^{-2}.

2D slices of predictions from SM trained with data from the 50 experiments performed are shown in Figure 3C-E. The predicted j_{CO} are shown in Figure 3C at j_{act} = 100 and 300 mA cm^{-2}. For j_{act} = 300 mA cm^{-2}, the predicted maximum j_{CO} was at t_{act} = 545 ms and t_{rest} = 48 ms, while for j_{act} of 100 mA cm^{-2}, the optimum j_{CO} was at t_{act} = 545 ms and t_{rest} = 10ms. As j_{act} increases, the predicted maximum j_{CO} increased from 53.5 to 119 mA cm^{-2}. These results agree with the results from the 2D experiments, in which the t_{act}/t_{rest} ratio and j_{CO} increase together. The FE_{CO} predictions are shown in Figure 3D. At j_{act} = 100 mA cm^{-2}, the maximum FE_{CO} is predicted to be 0.83 at t_{act} = 1500 ms and t_{rest} = 736 ms. As j_{act} increases, the location in the pulse time design space of the maximum FE_{CO} shifts towards a

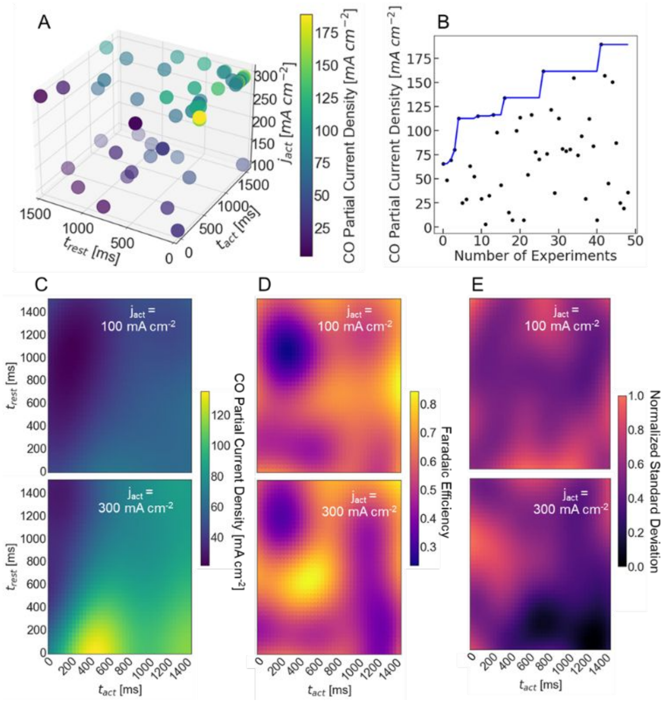

Figure 3. (A) Location in 3D design space of the 50 experimental conditions studied in the optimization campaign, varying j_{act}, t_{act}, and t_{rest}. Color of the marker indicates the CO partial current density at that condition. (B) CO partial current density throughout the optimization campaign. Black markers indicate the experimental points and the blue line indicates the highest value achieved. (C-E) 2D slices at j_{act} = 100 mA cm^{-2} and 300 mA cm^{-2} showing the GPR predictions of (C) CO partial current density, (D) CO_{FE}, and (E) normalized standard deviation, based on the 50 observed experiments. Resting current density was set to 0 mA/cm^2.

shorter t_{act}. This results in the predicted maximum FE_{CO} at j_{act} = 300 mA cm^{-2} to be 0.84 at t_{act} = 583 ms and t_{rest} = 660 ms. The shift towards shorter t_{act} at higher j_{act} is likely due to the faster depletion of CO_2 which results in the need for lower t_{act} to not deplete the CO_2 concentration at or near the electrocatalyst surface. In order to provide insights into the prediction accuracy of the GPR SM, Figure 3E shows the normalized standard deviation of the predictions throughout the design space. At j_{act} = 100 mA cm^{-2}, the predictions in a large fraction of the space have near-average standard deviations due to extensive exploration around this j_{act} by the BO algorithm, while at 300 mA cm^{-2}, accurate predictions are mostly concentrated near the optimal conditions due to the large numbers of experiments performed around optimal conditions during the exploitation stage of BO.

4D optimization of CO partial current density

Having identified optimal t_{act}, t_{rest}, and j_{act} with a fixed resting current density, j_{rest} = 0 mA cm^{-2}, the next step in the optimization was to explore possible improvements by modulating j_{rest}. Figure 4A presents the 50 experimental conditions tested in the entire design space, showing a few conditions dispersed in the entire design space that were selected during the exploration stage of BO, and a concentration of experiments near high j_{act} and t_{act}, and low t_{rest} during the exploitation stage when the algorithm seeks to identify the optimal conditions. Figure 4B displays the improvement in j_{CO} as a function of experiments performed and identifies conditions that lead to a CO partial current density of 166 mA cm^{-2} after the 50 experiments. It must be noted that this j_{CO} is lower than the one found in the 3D optimization campaign with the same number of experiments. This suggests that the increased dimensionality of the optimization problem requires a larger number of experiments to approach the optimum. Furthermore, our results demonstrate that the impact of j_{rest} is not significant in the performance of the reactor, possibly because optimal t_{rest} values are small and thus any change in j_{rest} would only impact a small fraction of the operation time. These results underscore the need to carefully select optimization parameters so that the tradeoff between potential performance improvements and the need for larger experimental campaigns is balanced.

To gain insights into the effects of the 4 optimization parameters on the CO partial current density, Figure 4C shows the SM predictions of j_{CO} as 2D slices at the optimal location of the other two variables. These results are consistent with those of the 2D and 3D optimizations, where the high j_{CO} values are found at low t_{rest}, and high t_{act}, and j_{act}. 2D slices of the FE_{CO} predictions are shown in Figure 4D. The trends observed for FE_{CO} predictions are different than for j_{CO}, with high FE_{CO} found at low t_{rest}, t_{act} and j_{act}. Figure 4E shows the standard deviations from the SM predictions of the 2D slices. As observed from the results, the increase in dimensionality results in larger standard deviations for a large fraction of the design space, underscoring the need for large datasets when the number of optimization parameters increase.

Conclusions

The study described above introduces a BO methodology to improve the performance of dynamic electrochemical conversion devices for electrons-to-molecules conversions. This

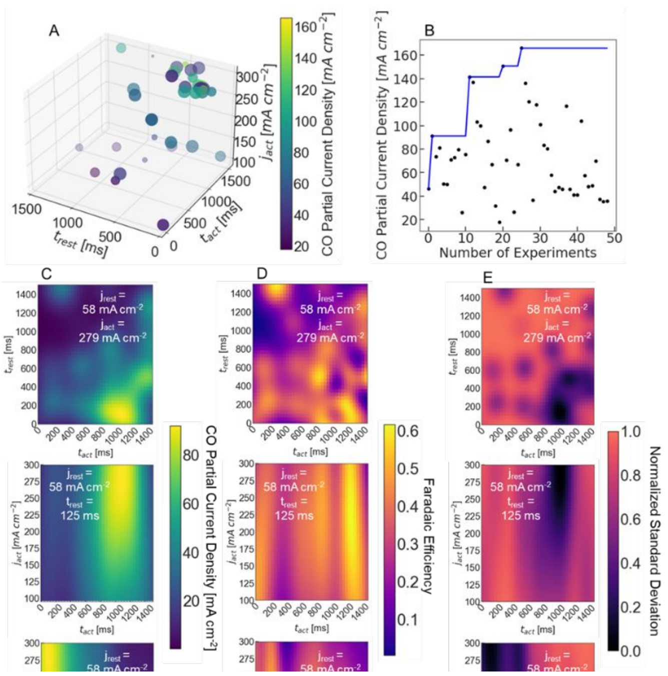

Figure 4. (A) Location in the 4D design space of the 50 experimental conditions studied in the optimization campaign, varying j_{act}, t_{act}, and t_{rest}. Size of the marker indicates the j_{rest} value and the color of the marker indicates the CO partial current density at that condition. (B) CO partial current density throughout the optimization campaign. Black markers indicate the experimental points and the blue line indicates the highest value achieved. (C-E) 2D slices at the optimal locations for CO partial current density of the other two variables, which are shown on the graph. The slices show the GPR predictions of (C) CO partial current density, (D) CO_{FE}, and (E) normalized standard deviation, based on the 50 observed experiments.

methodology allowed us to identify pulsed operation regimes in a CO_2 electrolyzer with improved selectivity and production rates. 3D optimization of t_{rest}, t_{act} and j_{act} with only 50 experiments showed improvements from j_{CO} = 115 mA cm^{-2} in the initial set of 10 experiments, to a maximum of 189 mA cm^{-2}. In the case of 4D optimization of t_{rest}, t_{act}, j_{act} and j_{rest}, the optimization campaign achieved an improvement from j_{CO} = 91 mA cm^{-2} in the initial set of 10 experiments, to a maximum of j_{CO} = 166 mA cm^{-2}. Because of the lower optimum value discovered in the 4D optimization, the 50 experiments in this case were not as effective at searching the design space as the 3D optimization. This result underscores the need for larger datasets at higher dimensions, and the need to carefully select optimization variables or to implement dimensionality reduction approaches (*e.g.*, principal component analysis) to minimize the number of experiments required in high dimensionality space. Furthermore, the statistical GPR surrogate models used in the BO methodology allowed us to develop performance (*i.e.*, j_{CO} or FE_{CO}) maps covering conditions beyond the ones tested. These maps provide further insights into the behavior of electrochemical devices across the parameter space. While this study focused on implementing a BO methodology for pulsed CO_2 electrolyzers in a 3 and 4D parameter space, BO can be easily extended to optimize other operational parameters such as potentials, gas flowrates, pressure and temperatures. Similar BO methods may also prove useful to optimize materials used as electrodes, electrocatalyst layers, and membranes but modifying these device parameters is more complex and would require innovative approaches to achieve high-throughput device assembly and testing. Integrating the BO framework presented here with high-throughput experimentation tools could enable rapid optimization of other electrochemical devices for the production of high-value chemicals that require complex reactions and the delicate control of the electrode microenvironment.

Data Availability Statement

The code used for running the optimization and the resulting data are provided in a Github repository with DOI 10.5281/zenodo.6354517.

Author Contributions

Daniel Frey: Conceptualization, Formal analysis, Investigation, Methodology, Software, Visualization, Writing – original draft **K.C. Neyerlin**: Writing – review & editing, Supervision, Funding acquisition, Methodology, Project administration **Miguel A. Modestino**: Conceptualization, Funding acquisition, Methodology, Project administration, Supervision, Writing – review & editing

Conflicts of interest

MAM is a director and has a financial interest in Sunthetics, Inc., a start-up company in the machine learning optimization space.

Acknowledgements

This work was authored in part by Alliance for Sustainable Energy, LLC, the manager and operator of the National Renewable Energy Laboratory for the U.S. Department of Energy (DOE) under Contract No. DE-AC36-08GO28308. Funding provided by the Office of Science Graduate Student Research program under Contract No. DE-SC0014664. The views expressed in the article do not necessarily represent the views of the DOE or the U.S. Government. The U.S. Government retains and the publisher, by accepting the article for publication, acknowledges that the U.S. Government retains a nonexclusive, paid-up, irrevocable, worldwide license to publish or reproduce the published form of this work, or allow others to do so, for U.S. Government purposes.

References

1. Blanco DE, Modestino MA. Organic electrosynthesis for sustainable chemical manufacturing. Trends in Chemistry. 2019;1(1):8-10.
2. Biddinger EJ, Modestino MA. Electro-organic syntheses for green chemical manufacturing. Electrochem Soc Interface. 2020;29:43-7.
3. Schiffer ZJ, Limaye AM, Manthiram K. Thermodynamic Discrimination between Energy Sources for Chemical Reactions. Joule. 2021;5(1):135-48.
4. De Luna P, Hahn C, Higgins D, Jaffer SA, Jaramillo TF, Sargent EH. What would it take for renewably powered electrosynthesis to displace petrochemical processes? Science. 2019;364(6438).
5. Brueske S, Kramer C, Fisher A. Bandwidth Study on Energy Use and Potential Energy Saving Opportunities in US Chemical Manufacturing. Energetics; 2015.
6. Xue D, Balachandran PV, Hogden J, Theiler J, Xue D, Lookman T. Accelerated search for materials with targeted properties by adaptive design. Nat Commun. 2016;7(1):1-9.
7. Vahid A, Rana S, Gupta S, Vellanki P, Venkatesh S, Dorin T. New bayesian-optimization-based design of high-strength 7xxx-series alloys from recycled aluminum. JOM. 2018;70(11):2704-9.
8. Li C, de Celis Leal DR, Rana S, Gupta S, Sutti A, Greenhill S, et al. Rapid Bayesian optimisation for synthesis of short polymer fiber materials. Scientific reports. 2017;7(1):1-10.
9. Abdelrahman H, Berkenkamp F, Poland J, Krause A. Bayesian optimization for maximum power point tracking in photovoltaic power plants. 2016 European Control Conference (ECC). 2016:2078-83.
10. Kikuchi S, Oda H, Kiyohara S, Mizoguchi T. Bayesian optimization for efficient determination of metal oxide grain boundary structures. Physica B: Condensed Matter. 2018;532:24-8.
11. Khajah MM, Roads BD, Lindsey RV, Liu Y-E, Mozer MC. Designing engaging games using Bayesian optimization. Proceedings of the 2016 CHI conference on human factors in computing systems. 2016:5571-82.
12. Lorenz R, Violante IR, Monti RP, Montana G, Hampshire A, Leech R. Dissociating frontoparietal brain networks with neuroadaptive Bayesian optimization. Nat Commun. 2018;9(1):1-14.
13. Frey D, Shin J, Musco C, Modestino MA. Chemically-informed data-driven optimization (ChIDDO): Leveraging physical models and Bayesian learning to accelerate chemical research. Reaction Chemistry & Engineering. 2022.
14. Frazier P. A tutorial on Bayesian optimization. arXiv: 180702811. 2018.

15. Herbol HC, Hu W, Frazier P, Clancy P, Poloczek M. Efficient search of compositional space for hybrid organic–inorganic perovskites via Bayesian optimization. Computational Materials. 2018;4(1):1-7.
16. Herbol HC, Poloczek M, Clancy P. Cost-effective materials discovery: Bayesian optimization across multiple information sources. Materials Horizons. 2020.
17. Yamashita T, Sato N, Kino H, Miyake T, Tsuda K, Oguchi T. Crystal structure prediction accelerated by Bayesian optimization. Physical Review Materials. 2018;2(1):013803.
18. Ju S, Shiga T, Feng L, Hou Z, Tsuda K, Shiomi J. Designing nanostructures for phonon transport via Bayesian optimization. Physical Review X. 2017;7(2):021024.
19. Ueno T, Rhone TD, Hou Z, Mizoguchi T, Tsuda K. COMBO: an efficient Bayesian optimization library for materials science. Materials discovery. 2016;4:18-21.
20. Hashimoto W, Tsuji Y, Yoshizawa K. Optimization of Work Function via Bayesian Machine Learning Combined with First-Principles Calculation. The Journal of Physical Chemistry C. 2020;124(18):9958-70.
21. Balachandran PV, Kowalski B, Sehirlioglu A, Lookman T. Experimental search for high-temperature ferroelectric perovskites guided by two-step machine learning. Nat Commun. 2018;9(1):1-9.
22. Higgins K, Valleti SM, Ziatdinov M, Kalinin SV, Ahmadi M. Chemical Robotics Enabled Exploration of Stability in Multicomponent Lead Halide Perovskites via Machine Learning. ACS Energy Lett. 2020;5(11):3426-36.
23. Ling J, Hutchinson M, Antono E, Paradiso S, Meredig B. High-dimensional materials and process optimization using data-driven experimental design with well-calibrated uncertainty estimates. Integrating Materials and Manufacturing Innovation. 2017;6(3):207-17.
24. MacLeod BP, Parlane FG, Morrissey TD, Häse F, Roch LM, Dettelbach KE, et al. Self-driving laboratory for accelerated discovery of thin-film materials. Science Advances. 2020;6(20):eaaz8867.
25. Min K, Cho E. Accelerated discovery of potential ferroelectric perovskite via active learning. Journal of Materials Chemistry C. 2020;8(23):7866-72.
26. Park S, Na J, Kim M, Lee JM. Multi-objective Bayesian optimization of chemical reactor design using computational fluid dynamics. Comput Chem Eng. 2018;119:25-37.
27. Schweidtmann AM, Clayton AD, Holmes N, Bradford E, Bourne RA, Lapkin AA. Machine learning meets continuous flow chemistry: Automated optimization towards the Pareto front of multiple objectives. Chem Eng J. 2018;352:277-82.
28. Burger B, Maffettone PM, Gusev VV, Aitchison CM, Bai Y, Wang X, et al. A mobile robotic chemist. Nature. 2020;583(7815):237-41.
29. Granda JM, Donina L, Dragone V, Long D-L, Cronin L. Controlling an organic synthesis robot with machine learning to search for new reactivity. Nature. 2018;559(7714):377-81.
30. Guo Z, Wu S, Ohno M, Yoshida R. Bayesian Algorithm for Retrosynthesis. Journal of Chemical Information and Modeling. 2020;60(10):4474-86.
31. Häse F, Roch LM, Aspuru-Guzik A. Chimera: enabling hierarchy based multi-objective optimization for self-driving laboratories. Chemical science. 2018;9(39):7642-55.
32. Häse F, Roch LM, Aspuru-Guzik A. Next-generation experimentation with self-driving laboratories. Trends in Chemistry. 2019;1(3):282-91.
33. Kondo M, Wathsala H, Sako M, Hanatani Y, Ishikawa K, Hara S, et al. Exploration of flow reaction conditions using machine-learning for enantioselective organocatalyzed Rauhut–Currier and [3+ 2] annulation sequence. Chem Commun. 2020;56(8):1259-62.
34. Shields BJ, Stevens J, Li J, Parasram M, Damani F, Alvarado JIM, et al. Bayesian reaction optimization as a tool for chemical synthesis. Nature. 2021;590(7844):89-96.
35. Reker D, Hoyt EA, Bernardes GJ, Rodrigues T. Adaptive Optimization of Chemical Reactions with Minimal Experimental Information. Cell Reports Physical Science. 2020;1(11):100247.
36. Kim K, Lee WH, Na J, Hwang Y, Oh H-S, Lee U. Data-driven pilot optimization for electrochemical CO mass production. Journal of Materials Chemistry A. 2020;8(33):16943-50.
37. Wang Y, Xie T, France-Lanord A, Berkley A, Johnson JA, Shao-Horn Y, et al. Toward Designing Highly Conductive Polymer Electrolytes by Machine Learning Assisted Coarse-Grained Molecular Dynamics. Chem Mater. 2020;32(10):4144-51.
38. Attia PM, Grover A, Jin N, Severson KA, Markov TM, Liao Y-H, et al. Closed-loop optimization of fast-charging protocols for batteries with machine learning. Nature. 2020;578(7795):397-402.
39. Doan HA, Agarwal G, Qian H, Counihan MJ, Rodríguez-López J, Moore JS, et al. Quantum Chemistry-Informed Active Learning to Accelerate the Design and Discovery of Sustainable Energy Storage Materials. Chem Mater. 2020.
40. Dave A, Mitchell J, Kandasamy K, Wang H, Burke S, Paria B, et al. Autonomous Discovery of Battery Electrolytes with Robotic Experimentation and Machine Learning. Cell Reports Physical Science. 2020:100264.
41. Jouny M, Luc W, Jiao F. General techno-economic analysis of CO2 electrolysis systems. Industrial & Engineering Chemistry Research. 2018;57(6):2165-77.
42. Bushuyev OS, De Luna P, Dinh CT, Tao L, Saur G, van de Lagemaat J, et al. What should we make with CO2 and how can we make it? Joule. 2018;2(5):825-32.
43. Lee J, Lee W, Ryu KH, Park J, Lee H, Lee JH, et al. Catholyte-free electroreduction of CO 2 for sustainable production of CO: concept, process development, techno-economic analysis, and CO 2 reduction assessment. Green Chemistry. 2021;23(6):2397-410.
44. Rumayor M, Dominguez-Ramos A, Perez P, Irabien A. A techno-economic evaluation approach to the electrochemical reduction of CO2 for formic acid manufacture. Journal of CO2 Utilization. 2019;34:490-9.
45. Somoza-Tornos A, Guerra OJ, Crow AM, Smith WA, Hodge B-M. Process modeling, techno-economic assessment, and life cycle assessment of the electrochemical reduction of CO2: a review. Iscience. 2021:102813.
46. Grim RG, Huang Z, Guarnieri MT, Ferrell JR, Tao L, Schaidle JA. Transforming the carbon economy: challenges and opportunities in the convergence of low-cost electricity and reductive CO 2 utilization. Energy Environ Sci. 2020;13(2):472-94.
47. Ma S, Lan Y, Perez GM, Moniri S, Kenis PJ. Silver supported on titania as an active catalyst for electrochemical carbon dioxide reduction. ChemSusChem. 2014;7(3):866-74.
48. Hoshi N, Kato M, Hori Y. Electrochemical reduction of CO2 on single crystal electrodes of silver Ag (111), Ag (100) and Ag (110). J Electroanal Chem. 1997;440(1-2):283-6.
49. Hori Y, Ito H, Okano K, Nagasu K, Sato S. Silver-coated ion exchange membrane electrode applied to electrochemical reduction of carbon dioxide. Electrochim Acta. 2003;48(18):2651-7.
50. Kim C, Jeon HS, Eom T, Jee MS, Kim H, Friend CM, et al. Achieving selective and efficient electrocatalytic activity for CO2 reduction using immobilized silver nanoparticles. Journal of the American Chemical Society. 2015;137(43):13844-50.
51. Delacourt C, Ridgway PL, Kerr JB, Newman J. Design of an electrochemical cell making syngas (CO+ H2) from CO2 and H2O reduction at room temperature. J Electrochem Soc. 2007;155(1):B42.

52. Jiang K, Kharel P, Peng Y, Gangishetty MK, Lin H-YG, Stavitski E, et al. Silver nanoparticles with surface-bonded oxygen for highly selective CO2 reduction. ACS Sustainable Chemistry & Engineering. 2017;5(10):8529-34.
53. Salvatore DA, Weekes DM, He J, Dettelbach KE, Li YC, Mallouk TE, et al. Electrolysis of Gaseous CO2 to CO in a Flow Cell with a Bipolar Membrane. ACS Energy Lett. 2017;3(1):149-54.
54. Vermaas DA, Smith WA. Synergistic electrochemical CO2 reduction and water oxidation with a bipolar membrane. ACS Energy Lett. 2016;1(6):1143-8.
55. Shiratsuchi R, Nogami G. Pulsed electroreduction of CO 2 on silver electrodes. J Electrochem Soc. 1996;143(2):582.
56. Yano H, Shirai F, Nakayama M, Ogura K. Electrochemical reduction of CO2 at three-phase (gas| liquid| solid) and two-phase (liquid| solid) interfaces on Ag electrodes. J Electroanal Chem. 2002;533(1-2):113-8.
57. Kim YE, Kim B, Lee W, Ko YN, Youn MH, Jeong SK, et al. Highly tunable syngas production by electrocatalytic reduction of CO2 using Ag/TiO2 catalysts. Chem Eng J. 2021;413:127448.
58. Lee WH, Ko Y-J, Choi Y, Lee SY, Choi CH, Hwang YJ, et al. Highly selective and scalable CO2 to CO-Electrolysis using coral-nanostructured Ag catalysts in zero-gap configuration. Nano Energy. 2020;76:105030.
59. Oh S, Park YS, Park H, Kim H, Jang JH, Choi I, et al. Ag-deposited Ti gas diffusion electrode in proton exchange membrane CO2 electrolyzer for CO production. Journal of Industrial and Engineering Chemistry. 2020;82:374-82.
60. Sun D, Xu X, Qin Y, Jiang SP, Shao Z. Rational Design of Ag-Based Catalysts for the Electrochemical CO2 Reduction to CO: A Review. ChemSusChem. 2020;13(1):39-58.
61. Dinh C-T, Burdyny T, Kibria MG, Seifitokaldani A, Gabardo CM, De Arquer FPG, et al. CO2 electroreduction to ethylene via hydroxide-mediated copper catalysis at an abrupt interface. Science. 2018;360(6390):783-7.
62. Kwon Y, Lum Y, Clark EL, Ager JW, Bell AT. CO2 electroreduction with enhanced ethylene and ethanol selectivity by nanostructuring polycrystalline copper. ChemElectroChem. 2016;3(6):1012-9.
63. Yang HJ, Yang H, Hong YH, Zhang PY, Wang T, Chen LN, et al. Promoting ethylene selectivity from CO2 electroreduction on CuO supported onto CO2 capture materials. ChemSusChem. 2018;11(5):881-7.
64. Yang P-P, Zhang X-L, Gao F-Y, Zheng Y-R, Niu Z-Z, Yu X, et al. Protecting copper oxidation state via intermediate confinement for selective CO2 electroreduction to C2+ fuels. Journal of the American Chemical Society. 2020;142(13):6400-8.
65. Kibria MG, Dinh CT, Seifitokaldani A, De Luna P, Burdyny T, Quintero-Bermudez R, et al. A surface reconstruction route to high productivity and selectivity in CO2 electroreduction toward C2+ hydrocarbons. Adv Mater. 2018;30(49):1804867.
66. Winiwarter A, Silvioli L, Scott SB, Enemark-Rasmussen K, Sariç M, Trimarco DB, et al. Towards an atomistic understanding of electrocatalytic partial hydrocarbon oxidation: propene on palladium. Energy Environ Sci. 2019;12(3):1055-67.
67. Xie J, Zhang Q, Chuang KT. An IGC study of Pd/SDB catalysts for partial oxidation of propylene to acrylic acid. J Catal. 2000;191(1):86-92.
68. Casebolt R, Levine K, Suntivich J, Hanrath T. Pulse check: Potential opportunities in pulsed electrochemical CO2 reduction. Joule. 2021.
69. Blanco DE, Lee B, Modestino MA. Optimizing organic electrosynthesis through controlled voltage dosing and artificial intelligence. Proceedings of the National Academy of Sciences. 2019;116(36):17683-9.
70. Kim C, Bui JC, Luo X, Cooper JK, Kusoglu A, Weber AZ, et al. Tailored catalyst microenvironments for CO2 electroreduction to multicarbon products on copper using bilayer ionomer coatings. Nat Energy. 2021;6(11):1026-34.
71. Shiratsuchi R, Aikoh Y, Nogami G. Pulsed electroreduction of CO 2 on copper electrodes. J Electrochem Soc. 1993;140(12):3479.
72. Nogami G, Itagaki H, Shiratsuchi R. Pulsed Electroreduction of CO 2 on Copper Electrodes-II. J Electrochem Soc. 1994;141(5):1138.
73. Ishimaru S, Shiratsuchi R, Nogami G. Pulsed Electroreduction of CO 2 on Cu-Ag Alloy Electrodes. J Electrochem Soc. 2000;147(5):1864.
74. Yano J, Morita T, Shimano K, Nagami Y, Yamasaki S. Selective ethylene formation by pulse-mode electrochemical reduction of carbon dioxide using copper and copper-oxide electrodes. J Solid State Electrochem. 2007;11(4):554-7.
75. Kumar B, Brian JP, Atla V, Kumari S, Bertram KA, White RT, et al. Controlling the product syngas H2: CO ratio through pulsed-bias electrochemical reduction of CO2 on copper. ACS Catalysis. 2016;6(7):4739-45.
76. Jännsch Y, Leung JJ, Hämmerle M, Magori E, Wiesner-Fleischer K, Simon E, et al. Pulsed potential electrochemical CO2 reduction for enhanced stability and catalyst reactivation of copper electrodes. Electrochem Commun. 2020;121:106861.
77. Arán-Ais RM, Scholten F, Kunze S, Rizo R, Cuenya BR. The role of in situ generated morphological motifs and Cu (I) species in C 2+ product selectivity during CO 2 pulsed electroreduction. Nat Energy. 2020;5(4):317-25.
78. Engelbrecht A, Uhlig C, Stark O, Hämmerle M, Schmid G, Magori E, et al. On the electrochemical CO2 reduction at copper sheet electrodes with enhanced long-term stability by pulsed electrolysis. J Electrochem Soc. 2018;165(15):J3059.
79. Strain JM, Gulati S, Pishgar S, Spurgeon JM. Pulsed Electrochemical Carbon Monoxide Reduction on Oxide-Derived Copper Catalyst. ChemSusChem. 2020;13(11):3028-33.
80. Casebolt R, Kimura KW, Levine K, Cimada DaSilva JA, Kim J, Dunbar TA, et al. Effect of electrolyte composition and concentration on pulsed potential electrochemical CO2 reduction. ChemElectroChem. 2021;8(4):681-8.
81. Kimura KW, Casebolt R, Cimada DaSilva J, Kauffman E, Kim J, Dunbar TA, et al. Selective electrochemical CO2 reduction during pulsed potential stems from dynamic interface. ACS Catalysis. 2020;10(15):8632-9.
82. Kimura KW, Fritz KE, Kim J, Suntivich J, Abruña HD, Hanrath T. Controlled Selectivity of CO2 Reduction on Copper by Pulsing the Electrochemical Potential. ChemSusChem. 2018;11(11):1781-6.
83. Xu Y, Edwards JP, Liu S, Miao RK, Huang JE, Gabardo CM, et al. Self-cleaning CO2 reduction systems: unsteady electrochemical forcing enables stability. ACS Energy Lett. 2021;6(2):809-15.
84. Park AM, Owczarczyk ZR, Garner L, Yang-Neyerlin AC, Long H, Antunes C, et al. Synthesis and characterization of perfluorinated anion exchange membranes. ECS Transactions. 2017;80(8):957.
85. Cardoso TN, Silva RM, Canuto S, Moro MM, Gonçalves MA. Ranked batch-mode active learning. Information Sciences. 2017;379:313-37.
86. Frey D. Bayesian-Optimization-of-Electrochemical-Devices-for-Electrons-to-Molecules-Conversions-. GitHub repository. 2022.

